Perovskite Electrode

Rapid Fabrication of Electrodes for Symmetrical Solid Oxide Cells by Extreme Heat Treatment

Weiwei Fan*, Zhu Sun*, Manxi Wang, Manxian Li, and Yuming Chen* ID

Symmetrical solid oxide cells (SSOCs) are very useful for energy generation and conversion. To fabricate the electrode of SSOC, it is very time-consuming to use the conventional approach. In this work, we design and develop a novel method, extreme heat treatment (EHT), to rapidly fabricate electrodes for SSOC. We show that by using the EHT method, the electrode can be fabricated in seconds (the fastest method to date), benefiting from enhanced reaction kinetics. The EHT-fabricated electrode presents a porous structure and good adhesion with the electrolyte. In contrast, tens of hours are needed to prepare the electrode by the conventional approach, and the prepared electrode exhibits a dense structure with a larger particle size due to the lengthy treatment. The EHT-fabricated electrode shows desirable electrochemical performance. Moreover, we show that the electrocatalytic activity of the perovskite electrode can be tuned by the vigorous approach of fast exsolution, deriving from the increased active sites for enhancing the electrochemical reactions. At 900 °C, a promising peak power density of 966 mW cm^{-2} is reached. Our work exploits a new territory to fabricate and develop advanced electrodes for SSOCs in a rapid and high-throughput manner.

1. Introduction

Solid oxide cell (SOC), which can be operated in two modes with high efficiency, is an important technique for energy generation and convention.[1–6] One mode is the solid oxide fuel cell (SOFC), which can produce electricity in an environment-friendly manner by oxidizing fuel gas,[7–10] and the other mode is the solid oxide electrolysis cell (SOEC) which can generate hydrogen and oxygen via electrolyzing water[11,12] (**Figure 1**a). SOC consists of dense electrolytes that conduct ions (i.e. O^{2-} or H$^+$), porous anodes and cathodes that conduct both ions and electrons, and mixed ionic and electronic conductors (MIECs). Different from the traditional SOCs (anode and cathode are different materials), symmetrical solid oxide cells (SSOCs, anode and cathode are the same material) not only simplify the fabricating process but also minimize the compatibility issues coming from the interfaces of electrode/electrolyte.[13–15] Therefore, in recent years, SSOCs have attracted broad attention in the all-solid electrochemical cell field.[14,16,17]

Due to the sluggish diffusion of active species, it is generally tedious and time-consuming to prepare SSOC's electrode by the conventional approach.[18–23] To be more specific, first, the solid precursors need to be calcined for several or even tens of hours at high temperature to acquire the MIEC electrode powders with the desired phase. It is worth noting that, because of the low heating rate (Figure S1, Supporting Information) of the heating facility applied in the conventional approach, several hours are required to reach the calcining temperature, which greatly affects the efficiency of the electrode fabrication. Subsequently, the as-synthesized electrode powders are dispersed into a dispersant to form a slurry, which is then pasted on the airtight electrolyte. To obtain good contact between the electrode and the electrolyte, the printed ink needs to be sintered at a high temperature for several hours (Figure 1b). Due to the long-time sintering, the phenomenon of particle coarsening is usually severe, resulting in a decrease in the specific surface area of the working electrode and eventually affecting cell performance. Overall, limited by the heating and cooling ramp, achievable temperature, and low reaction kinetics, generally tens of hours are required to prepare the MIEC electrodes for SSOCs by the conventional approach,[16,17,24–26] greatly restricting the production and development of SSOCs.

From thermodynamics ($K = e^{-\Delta Go/(RT)}$) and kinetics ($k = Ae^{-Ea/(RT)}$) points of view,[27,28] to form a new solid phase through the solid-state reaction (Figure S2, Supporting Information), high reaction kinetics could be expected at high temperatures, profiting from the lifted driving force to expedite the solid reaction processes. In other words, if the system could bypass the low-efficiency reacting region and directly go into the high-efficiency reacting region, there stands a good chance to acquire the desired phase rapidly. Conventionally, the heating/cooling rate is generally less than 100 °C min^{-1}. However, a very high heating/cooling rate of $\sim 10^5$ K s^{-1} was recently

Prof. W. Fan
Key Laboratory of Energy Thermal Conversion and Control of Ministry of Education, School of Energy and Environment, Southeast University, Nanjing 210096, China
E-mail: fanww@seu.edu.cn
Department of Nuclear Science and Engineering, Massachusetts Institute of Technology, Cambridge, Massachusetts 02139, USA
Z. Sun
School of Materials Science and Engineering, Shanghai Jiao Tong University, 800 Dongchuan Road, Shanghai 200240, China
Zhangjiang Institute for Advanced Study (ZIAS), Shanghai Jiao Tong University, Shanghai 201210, China
E-mail: sunzhu2022@sjtu.edu.cn
M. Wang, M. Li, Prof. Y. Chen
College of Environmental Science and Engineering and College of Physics and Energy, Fujian Normal University, Fuzhou 350000, China
E-mail: yumingc126@126.com
ID The ORCID identification number(s) for the author(s) of this article can be found under https://doi.org/10.1002/eem2.12718.
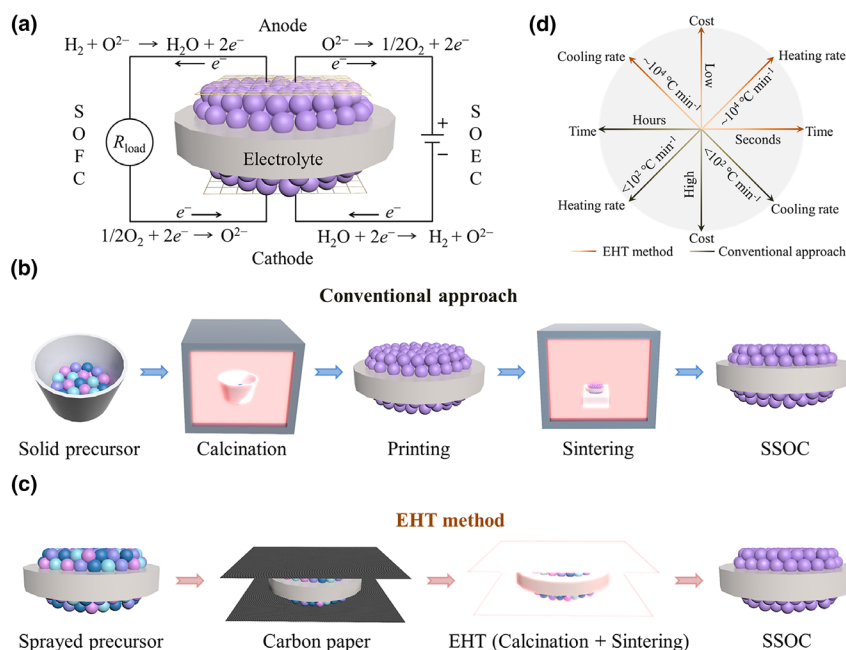
Figure 1. a) Schematic of the solid oxide cell (SOC). A solid oxide fuel cell can produce electricity by oxidizing a fuel. Regarding the solid oxide electrolysis cell, it can electrolyze water to generate hydrogen and oxygen gases. b) Workflow of the preparation of electrodes for symmetrical solid oxide cells (SSOC) by the conventional approach. c) Workflow of the fabrication of electrodes for SSOC by the EHT method. d) Comparison of the fabrication parameters between the EHT and the conventional methods.

reported[29] when using carbon nanofiber as a heater. Benefiting from the high temperature, up to octonary high-entropy-alloy nanoparticles were successfully synthesized. Therefore, we naturally question whether the electrodes of SSOCs could be rapidly obtained under extreme conditions.

In this work, with the motivation of fabricating electrodes for SSOCs in a rapid way, we designed and developed a novel recipe called extreme heat treatment (EHT). Considering that perovskite electrodes[30–32] are widely used for SSOCs because of their reasonable cost, MIEC property, and formidable structural stability,[33,34] perovskite electrodes were adopted as model materials. During explorations, we found that the eventual phase and microstructure of the electrodes were closely related to the texture of the carbon support applied. Herein, a customized carbon paper was applied as the heating source and support. Before conducting the EHT, fully mixed precursor ink was sprayed on the surface of the electrolyte, which was subsequently placed between the as-tailored carbon papers (Figure 1c and Figure S3, Supporting Information). We showed that after EHT for ~10 s at ~1600 °C, the EHT-fabricated electrode presented a single perovskite phase with a porous structure and good adhesion with the electrolyte, indicating that the working electrode could be successfully fabricated in seconds by the EHT method. However, it took more than 40 h to prepare the electrode using the conventional approach (Figure 1d). Benefiting from the short-time treatment, the EHT-fabricated electrode showed a smaller particle size as compared to that prepared by the conventional approach. Moreover, the EHT-fabricated electrode showed promising electrochemical performance, and improved performance was achieved after post-treatment. This work establishes a new way of fabricating and screening electrodes for SSOCs.

2. Results and Discussion

2.1. Crystal Structure and Micromorphology of the EHT-Fabricated Electrodes

Considering that Ti-based perovskites[35–37] are broadly used in symmetrical solid oxide cells because of their favorable structure stability, Ti-based lanthanides with perovskite structures were selected as model materials in current study. To demonstrate the feasibility of rapidly fabricating electrodes for SSOCs by the EHT method, fully mixed $La_{0.43}Ca_{0.37}TiO_{3-\delta}$ (LCT) precursor ink was spray-printed on the surface of the electrolyte through a customized mask by MASTER airbrush (**Figure 2a**). After placing the cell in the home-made setup, an optimized current of ~19.5 A was supplied to the system via a precisely programmable power supply. During the EHT, the temperature rapidly reached ~1600 °C within ~4 s. Particularly, a rapid heating rate of ~10^4 °C min^{-1} could be attained by the EHT method, which is much higher than that of the conventional approach (usually less than 10^2 °C min^{-1}). After the EHT for several seconds, a series of characterizations were conducted on the EHT-fabricated electrodes. Here, it is worth noting that for fabricating electrodes for symmetrical solid oxide cells by the EHT method, the EHT parameters (such as temperature, time, carbon paper thickness, etc.) relate closely with the crystal structure, microstructure, and performance of the electrode products. For example, generally, long treating times can bring about large particles and dense electrodes, while short treating times can give rise to impurity phases, resulting in an inferior performance. By tuning EHT parameters, there stands a good chance to fabricate other types of perovskite electrodes.

For SSOCs, generally, the electrode's crystal structure has an intimate influence on the eventual electrochemical performance. Therefore, the XRD technique was performed to study the crystal phase of the EHT-prepared electrodes. Compared to that of the LCT precursor (Figures S4 and S5, Supporting Information), it was found that after ~10 s treatment, the main diffraction peak of the EHT-prepared LCT (LCT-EHT) shifted to a higher 2θ angle, accompanied by the formation of new peaks (Figure S6, Supporting Information). This finding implied that the solid-state reaction dynamically took place among the precursors during the EHT (Figure 2b). To acquire more information about the crystal structure of LCT-EHT, LCT oxide was also prepared by the conventional approach (LCT-Con). It was demonstrated that for obtaining the desired perovskite phase, two-step calcination of the mixed powders was needed, 1100 °C 20 h and 1350 °C 20 h, suggesting that the reaction kinetics were very slow. The results showed that the LCT-Con oxide possessed an orthorhombic structure (Figure 2c and Figure S7, Supporting Information). For more clarity, the XRD pattern of a fresh YSZ electrolyte was also measured. To our surprise, it was observed that apart from the diffraction peaks coming from the YSZ electrolyte, the rest of the peaks matched well with those of the LCT-Con, indicating that the electrode with a perovskite structure was successfully acquired after EHT for ~10 s. Moreover, no distinctly additional peaks were
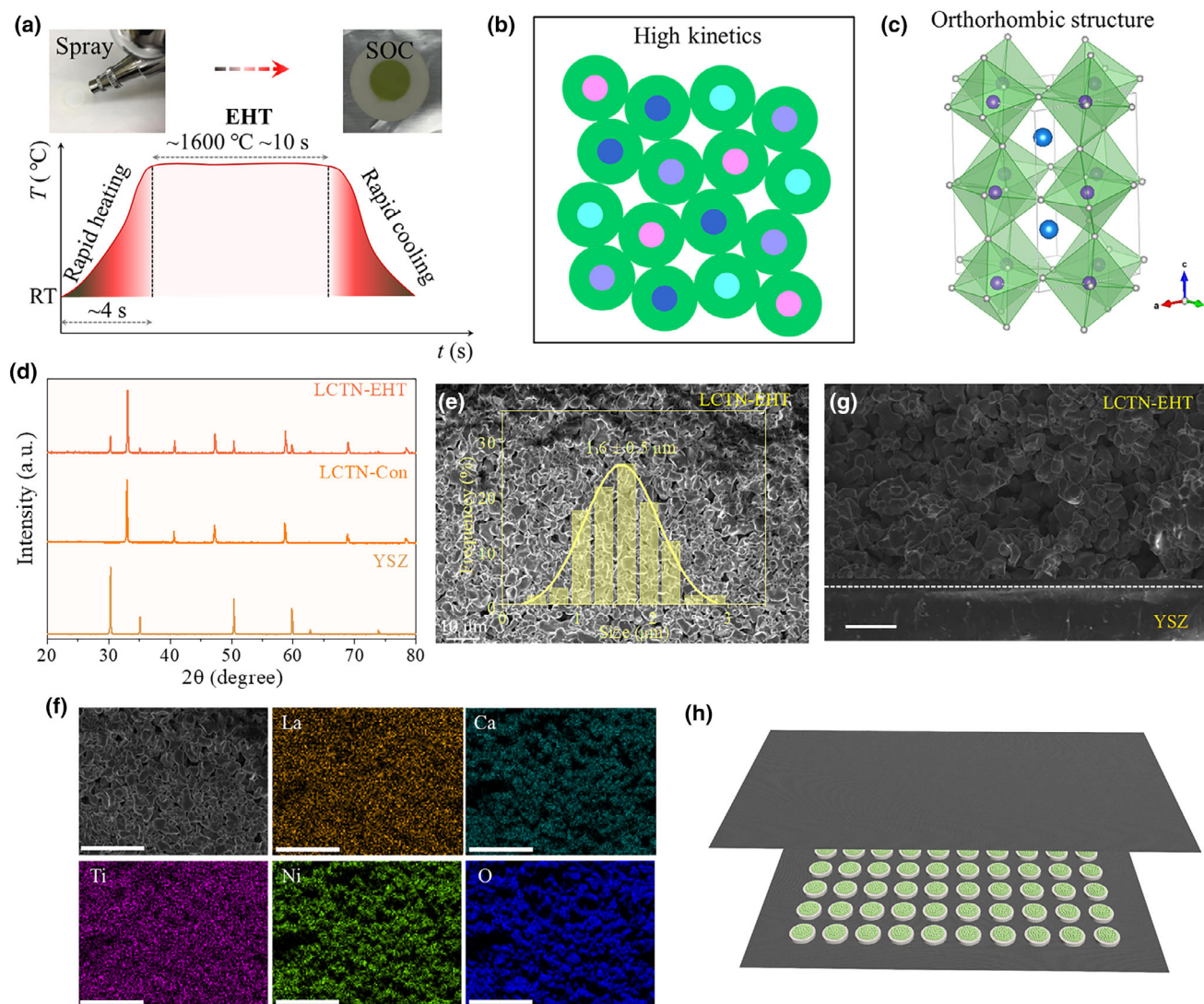
Figure 2. a) Temperature profile of the EHT method, picture of the spray printing, and the EHT-fabricated SSOC. b) Illustration of the formation of a new solid product among raw materials. A strong driving force can be supplied to the system by the EHT method, giving rise to a high reaction kinetics. c) Crystal structure of the LCT-EHT and LCTN-EHT perovskites, which can be represented by a 3D framework of BO_6 octahedrons filled with A-site cations in the interstitial space. Blue spheres represent La/Ca, purple spheres represent Ti/Ni, gray spheres represent O. d) XRD profile of the LCTN-EHT electrode. For comparison, the XRD profiles of LCTN-Con and YSZ are also shown. e) SEM image of the surface view of the LCTN-EHT electrode. The inset shows the corresponding particle size distribution. f) EDX mapping of the LCTN-EHT electrode. Scale bar is 20 μm. g) SEM image of the cross-section view of the LCTN-EHT electrode. Scale bar is 10 μm. h) Schematic of the fabrication of electrodes for SSOCs in a high-throughput way by the EHT method.

observed, suggesting that no detectable reaction took place between the electrode and the electrolyte and that they had good chemical compatibility.

Based on the defect chemistry, the electrocatalytic activity of the ABO_3-type perovskite electrodes can be tuned by doping other transition metal(s) at the B-site. Benefiting from the good catalytic activity and reasonable cost of nickel, Ni-doped perovskite electrodes are broadly applied in SSOCs.[24,38,39] Hence, a $La_{0.43}Ca_{0.37}Ti_{0.94}Ni_{0.06}O_{3-\delta}$ (LCTN) precursor (Figure S8, Supporting Information) was subsequently prepared and sprayed on the surface of the YSZ electrolyte to further inspect the capabilities of the EHT method. The result showed that after EHT for ~8 s, the measured XRD pattern was a superposition of the LCTN-Con and YSZ patterns (Figure 2d), indicating that an electrode with a perovskite orthorhombic structure was fabricated. Lattice parameters of $a = 5.4699$ Å, $b = 7.7373$ Å and $c = 5.4637$ Å were obtained for LCTN-EHT (Table S1, Supporting Information), which were similar to those of LCTN-Con (Table S2, Supporting Information), suggesting EHT is a promising approach to fabricating perovskite oxides. In principle, for different solid-state reactions, the energy barrier should be different, resulting in a difference in the treatment time.

The electrode's microstructure, relating to gas diffusion, adsorption, desorption, etc., is also important for the performance of SSOC. Therefore, SEM was conducted to inspect the micromorphology of the EHT-prepared electrode. The result showed that the LCTN-EHT electrode presented a porous structure (Figure 2e), which is beneficial for the electrochemical reactions occurring on the electrode. The average

3 of 8

particle size of the LCTN-EHT electrode was $1.6 \pm 0.5\,\mu m$. This was primarily due to the rapid treatment, which greatly limited particle growth. In contrast, the LCTN-Con electrode exhibited a dense microstructure, and the average particle size was $19 \pm 7\,\mu m$ (Figure S9, Supporting Information). Moreover, the EDX result verified the composition and good distribution of La, Ca, Ti, Ni and O elements for the LCTN-EHT electrode (Figure 2f).

In addition, for SSOCs, a good adhesion between the electrode and the electrolyte, associating closely with the charge transfer process, is necessary. Thus, the cross-section view of the EHT-fabricated electrode was inspected. The SEM result showed that the LCTN-EHT electrode adhered well to the standard electrolyte and no apparent delamination was detected (Figure 2g). Similarly, the LCT-EHT electrode also showed desirable microstructure and good adhesion (Figures S10–S12, Supporting Information), suggesting that the calcination and sintering procedures could be rapidly accomplished in one step by the EHT method. However, as to the conventional approach, it took more than 43 h to obtain the working electrode. Moreover, another beauty of the EHT method is that one can efficiently fabricate numerous cells through patterning the mask and tailoring the carbon paper (Figure 2h and Figures S13 and S14, Supporting Information). Overall, to fabricate electrodes for SSOC, tens of hours are required by the conventional approach, while only tens of seconds are needed by the EHT method, demonstrating that EHT is a powerful method to fabricate electrodes in a high-throughput manner.

2.2. Electrochemical Performance of the EHT-Fabricated Electrodes

Electrochemical impedance spectra (EIS) were applied to study the electrochemical properties of the EHT-fabricated electrodes. By using the home-made setup (Figure S15, Supporting Information), the EIS data were collected in the temperature range of 700–900 °C with an interval of 50 °C under open-circuit voltage (OCV). Regarding the EHT-fabricated LCT (LCT-EHT), a polarization resistance (R_p) of $99\,\Omega\,cm^2$ was obtained in humidified ($\sim$3% H_2O) hydrogen at 700 °C (**Figure 3**a), suggesting that the electrocatalytic activity of the LCT-EHT electrode was commonplace. With increasing the environmental temperature to 900 °C, the R_p value decreased to $7\,\Omega\,cm^2$, which was mainly ascribed to the thermal activation of the corresponding electrochemical reactions occurring on the electrode.[40] To investigate the stability of LCT-EHT, the R_p was monitored under OCV at 900 °C. During the measurement, no substantial change in the R_p value was detected (Figure 3b), suggesting that the stability of the EHT-fabricated electrode was desirable. Additionally, the redox-cycling performance of LCT-EHT was also investigated at 900 °C. For one cycle, ultra-high-purity (UHP) hydrogen was first introduced into the chamber, and then the hydrogen was switched to UHP oxygen after flushing with UHP argon. After stabilization at each atmosphere, the EIS data was recorded. The results showed that the R_p value varied slightly under different cycles (Figure 3c), suggesting that the LCT-EHT had good redox stability. Subsequently, EIS measurements were conducted on the LCTN-EHT. The results showed that, compared to LCT-EHT, lower R_p values were attained for LCTN-EHT. Across the whole temperature range, the R_p value changed from 8.4 at 700 °C to $0.8\,\Omega\,cm^2$ at 900 °C (Figure 3d), implying enhanced electrocatalytic activity on hydrogen oxidation. This was primarily attributed to the additionally formed oxygen vacancies after nickel doping, resulting from the electrochemical oxidation of

hydrogen.[41] During the following operation, it was found that the R_p value decreased gradually at first and then reached a plateau (Figure 3e). At $\sim$20 h, the R_p value went down to $0.44\,\Omega\,cm^2$. The decrease in R_p is mainly derived from the exsolved nanocatalysts after the chemical gas treatment (Figure S16, Supporting Information), which could provide more active sites, thus enhancing the electrochemical oxidation of hydrogen.[42,43] When the exsolution process reached equilibrium, the R_p value came to a plateau concurrently. For comparison, a new cell was also prepared using the conventional approach. Briefly, LCTN precursors were first calcinated to achieve the target phase. The prepared ink was then printed and sintered on both sides of the electrolyte. The results showed that the R_p value varied between 51 and $4.4\,\Omega\,cm^2$ during the measurements (Figure S17, Supporting Information). This inferior catalytic activity was presumably ascribed to the dense structure and larger particle size of the LCTN-Con electrode, which were detrimental to gas diffusion and reactant transport. Figure 3f shows the hydrogen partial pressure dependence of R_p of the LCTN-EHT at different temperatures. The R_p exhibited a linear behavior, and the slope changed slightly at the measured temperatures, suggesting a gas diffusion process, which generally has weak dependence on the thermal activation.[44]

Since the catalysis primarily takes place on the exterior layers of the catalyst,[45,46] decorating nanoparticles on the support is an efficient approach to increasing the active sites, eventually enhancing the electrocatalytic activity of the electrode.[47–50] Therefore, to further improve the electrocatalytic activity of LCTN-EHT, we developed an advanced approach to prepare the exsolution-based nanoparticle-decorated materials. Essentially, the exsolution of nanoparticles from the perovskite lattice is a process of phase decomposition, and like the other kind of ion diffusion-controlled precipitation, thermal potential could be a driving force to trigger the exsolution/decomposition. A fast exsolution could be expected at a high temperature due to the strong driving force supplied to the system, which could enhance the exsolution kinetics. Surprisingly, it was found that after treatment for $\sim$10 s at $\sim$1400 °C in 5%H_2/N_2 atmosphere, a large number of nanoparticles with good spatial distribution formed on the surface of the LCTN-EHT support (Figures S18 and S19, Supporting Information). As expected, much lower R_p values were acquired for the treated LCTN-EHT, suggesting that the electrocatalytic activity of LCTN-EHT was significantly improved. As displayed in Figure 3g, with the increase in temperature from 700 to 900 °C, the R_p value went from 0.67 to $0.11\,\Omega\,cm^2$. The cell showed good stability during the operation (Figure S20, Supporting Information). To investigate the thermal-cycling performance of the treated LCTN-EHT, the R_p was recorded by cycling the environmental temperature. For one cycle, the environmental temperature was first decreased from 900 to 700 °C and then increased from 700 to 900 °C. During the measurements, a thermocouple was integrated close to the cell to monitor the real temperature. No remarkable variation of the R_p was observed during the cycling (Figure 3h), implying favorable thermal-cycling stability.

Activation energy (E_a) related to the electrochemical reaction mechanism is generally calculated from the following equation:

$$\log R_p = \log R_0 - \frac{E_a}{2.303RT} \tag{1}$$

An E_a value of 1.28 eV was attained for the LCT-EHT. As to the LCTN-EHT, an E_a value of 1.16 eV was achieved, while it reached
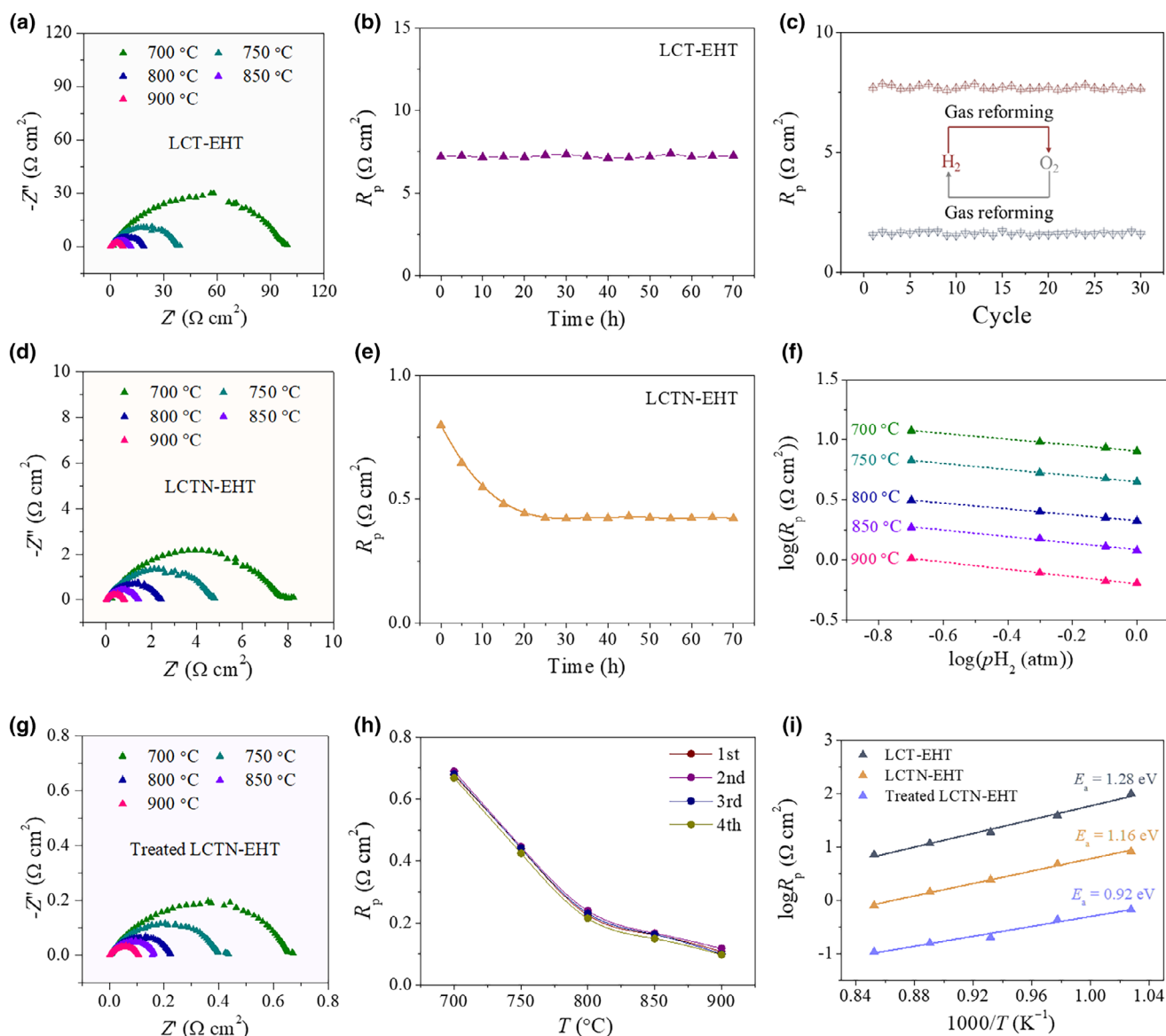
Figure 3. a) Nyquist plots of the EHT-fabricated LCT measured from 700 to 900 °C in wet (~3% H₂O) H₂ under OCV conditions. b) Time dependence of the R_p of LCT-EHT at 900 °C under OCV conditions. c) R_p of LCT-EHT collected under different redox cycles at 900 °C. d) Nyquist plots of the EHT-fabricated LCTN measured from 700 to 900 °C in wet (~3% H₂O) H₂ under OCV conditions. e) Time dependence of the R_p of LCTN-EHT at 900 °C under OCV conditions. f) Hydrogen partial pressure (pH_2) dependence of R_p for LCTN-EHT at different temperatures. g) Nyquist plots of the treated LCTN-EHT measured from 700 to 900 °C in wet (~3% H₂O) H₂ under OCV conditions. h) R_p of the treated LCTN-EHT collected under different thermal cycles in wet H₂. i) Arrhenius plots of R_p for the corresponding electrodes.

0.92 eV for the treated LCTN-EHT (Figure 3i), further demonstrating the enhancement of the electrochemical kinetics.

2.3. Full Cell Performance of the EHT-Fabricated Electrodes

In order to investigate the full cell performance of the EHT-fabricated electrodes, new cells were prepared in a high-throughput way. Subsequently, the cell was mounted on the home-made setup, coupled with gold meshes as the current collectors (**Figure 4a**). During the measurement, the anode chamber was filled with wet (~3% H₂O) hydrogen.

As shown in Figure 4b, an open-circuit voltage of ~1.1 V was achieved, indicating good sealing of the cell. At 700 °C, the EHT-fabricated LCT showed a low peak power density (PPD) of 1.4 mW cm⁻², implying that the electrochemical reactions occurring on the electrode were very sluggish. Due to the enhanced electrochemical kinetics, higher PPD values were attained at higher temperatures. At 900 °C, the PPD reached 22 mW cm⁻². During the following operation, the cell exhibited good stability, and the output varied slightly (Figure S21, Supporting Information).

As to the EHT-fabricated LCTN, the performance showed a mediocre improvement at the working temperatures. PPD values of 22,

5 of 8

45, 69, 93, and 116 mW cm^{-2} were acquired at 700, 750, 800, 850, and 900 °C (Figure 4c), respectively. At 900 °C, similarly, the PPD value increased gradually at the beginning, which was mainly attributed to the exsolved nanocatalysts with good catalytic activity. After operating ~20 h, a plateau appeared and the PPD value reached ~220 mW cm^{-2} (Figure S22, Supporting Information). With respect to the treated LCTN-EHT, a remarkable enhancement of the electrochemical performance was obtained in the temperature range of 700–900 °C (Figure 4d). A promising PPD value of 966 mW cm^{-2} was attained at 900 °C. Compared to the fresh LCTN-EHT, almost a 9-fold enhancement was attained (Figure 4e). Concurrently, the polarization resistance decreased prominently from 1.7 to 0.2 Ω cm^2 (Figure 4f,g, Figures S23 and S24, Supporting Information). Considering the other components of the cell were similar, the variation in electrochemical performance was most probably derived from the fuel electrode. In fact, the impressively exsolved nanocatalysts

contributed to the hydrogen oxidation. By comparison, it can be found that the cell performance acquired in this work is very competitive compared to that of the other cells (Figure S25, Supporting Information), suggesting that the fast exsolution is a fascinating way to tune the electrocatalytic activity of the perovskite materials. Besides, no obvious variation in cell performance was observed during the operation (Figure 4h).

For the electrochemical oxidation of hydrogen[51–53] as a whole, it can be expressed by Equation (2). Benefiting from the exsolved nanocatalysts with outstanding catalytic activity, the adsorption of hydrogen molecular ($H_2 \leftrightarrow 2H_{ads}$) and dissociation of hydrogen ($H \leftrightarrow H^+ + e^-$) can dynamically take place. In other words, the kinetics of dissociative adsorption of hydrogen can be prominently improved by the fast exsolution. Subsequently, the spillover of hydrogen atoms to the interface of the nanoparticle/support will proceed around the exsolved nanoparticles. In the meantime, the
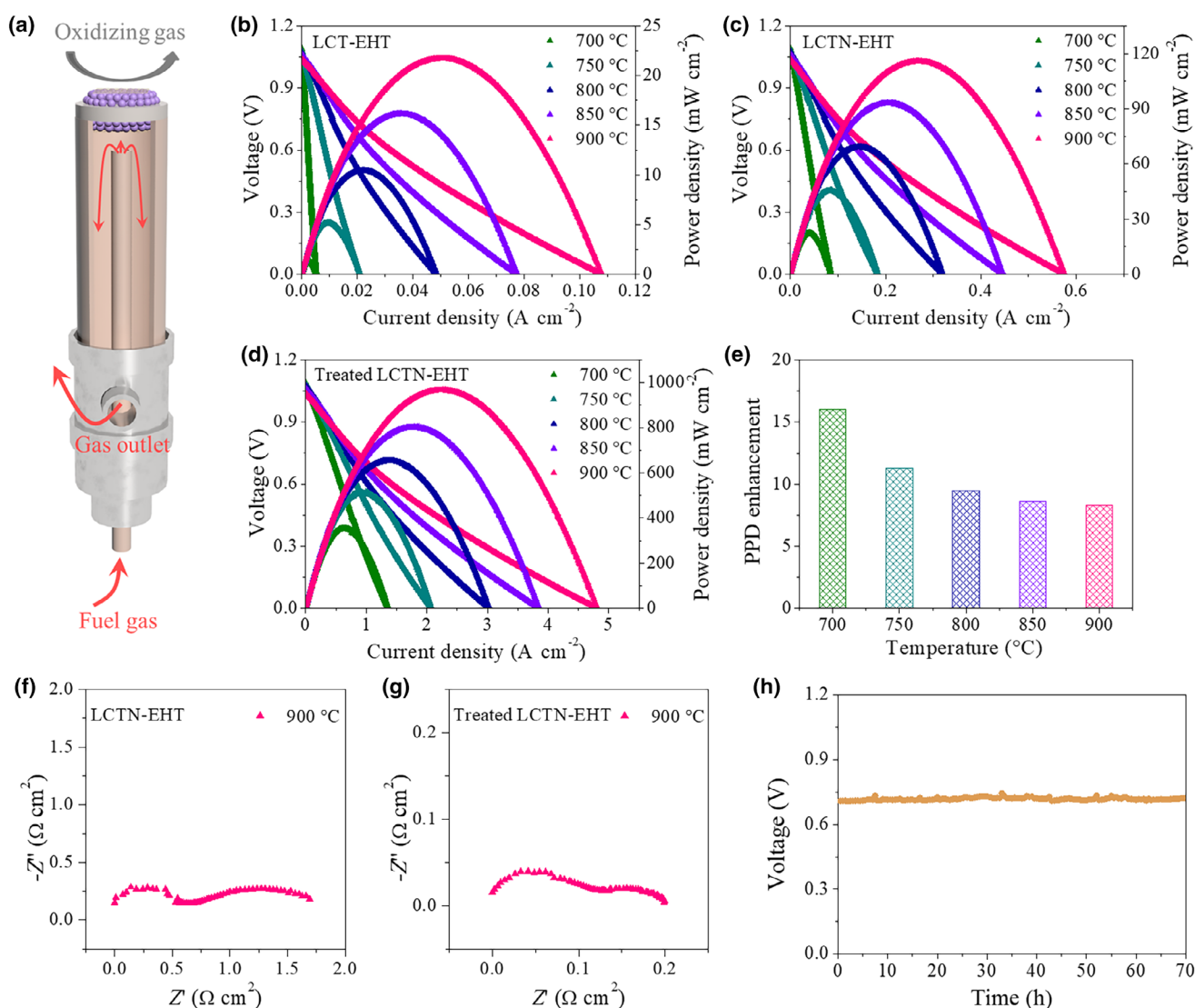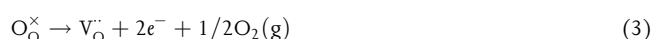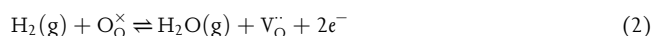

Figure 4. a) Schematic of the setup for the full cell performance test. $I-V(P)$ curves of the EHT-fabricated b) LCT and c) LCTN. d) $I-V(P)$ curves of the treated LCTN-EHT. e) Enhancement of peak power density of the treated LCTN-EHT compared to that of the fresh one. Nyquist plots of f) LCTN-EHT and g) the treated LCTN-EHT. h) Galvanostatic measurement of the treated LCTN-EHT under an applied current of 0.46 A cm^{-2} at 700 °C.

oxygen anions traverse from the other side to the fuel electrode through vacancy hopping and react with the hydrogen to form water $(2H^+ + O^{2-} \leftrightarrow H_2O)$. Actually, the exsolved nanoparticles can expand the reacting zone where the ions, electrons, and reactants meet together, synergistically facilitating the hydrogen oxidation reaction. Moreover, additional oxygen vacancies (Equation 3) will be generated during the exsolution to obey the rule of charge neutrality, which is also beneficial to the migration of oxygen anions. In a nutshell, EHT is a vigorous method to efficiently fabricate electrodes for SSOCs, enabling the development of all-solid electrochemical cells.

$$H_2(g) + O_O^{\times} \rightleftharpoons H_2O(g) + V_O^{\cdot\cdot} + 2e^- \tag{2}$$

$$O_O^{\times} \rightarrow V_O^{\cdot\cdot} + 2e^- + 1/2 O_2(g) \tag{3}$$

3. Conclusion

In this work, we developed a new method (EHT) to rapidly fabricate electrodes for symmetrical solid oxide cells (SSOCs). We showed that, benefiting from the strong driving force provided by the EHT method, electrodes could be prepared in seconds, the fastest method to date. The EHT-fabricated electrode showed a porous structure and good contact with the electrolyte. On the contrary, it required tens of hours to prepare the electrode by the conventional approach, and the electrode presented a dense structure with a larger particle size due to the lengthy treatment. We also reported that after the fast exsolution, the electrocatalytic activity of the perovskite electrode was remarkably improved, attributed to the additionally formed active sites. A PPD value of 966 mW cm^{-2} was achieved at 900 °C, almost 9 times higher than that of the fresh electrode. This study paves a new avenue to prepare and develop electrodes for SSOCs and other all-solid cells in a rapid mode.

4. Experimental Section

Ink fabrication: For La$_{0.43}$Ca$_{0.37}$TiO$_{3-\delta}$ (LCT) and La$_{0.43}$Ca$_{0.37}$Ti$_{0.94}$Ni$_{0.06}$O$_{3-\delta}$ (LCTN) precursors, raw materials of La$_2$O$_3$ (Sigma Aldrich), CaCO$_3$ (Sigma Aldrich), TiO$_2$ (Sigma Aldrich) and NiO (Sigma Aldrich) were carefully weighed by a high-precision electronic balance (Mettler Toledo). After ball milling in ethanol, the fully mixed precursor powders were dried on a hot plate at 80 °C. Subsequently, the as-prepared precursors and polyvinyl pyrrolidone (PVP) were mixed in ethanol by a Thinky stirrer. For the conventional approach, the mixed LCT and LCTN precursor powders were calcined in two steps (1100 °C 20 h and 1350 °C 20 h) in a tube furnace to obtain the target phase.

Cell fabrication: Before spraying the precursor ink, a polymer-based mask was manufactured into the desired shape and size and then covered on the standard YSZ electrolyte. The precursor ink was filled into a Master Airbrush Kit and sprayed on the surface of the electrolyte using Ar as the carrier gas. The gap between the nozzle and the electrolyte was about 1.5 cm. Carbon paper purchased from the Fuel Cell Store was fixed to the home-made setup and used as the heater. The as-sprayed cell was sandwiched between two carbon papers, which were connected to a remotely controllable power supply. A high current was supplied across the carbon papers to generate the Joule heating during the EHT.

Characterization: An X-ray diffractometer was applied to investigate the crystal phase of the EHT-fabricated electrodes as well as the materials prepared by the conventional approach. FEI Quanta 600F scanning electron microscopy was employed to study the micromorphology. For the fast exsolution, before introducing the nitrogen-balanced hydrogen, an integrated chamber coupled with the gas line and circuit was vacuumed by a pump; subsequently, the fast exsolution was conducted. An ultraviolet–visible spectrum collecting system was applied to

estimate the temperature. Electrochemical impedance spectroscopy (EIS) was collected (10^5–10^{-1} Hz) by Solartron 1260/1287, and the measured data were analyzed using the commercial software ZView. For the full cell performance measurements, the cells were carefully sealed on the top of the home-made setup with the high-temperature sealant.

Statistical analysis: The particle size distribution was acquired by measuring each particle on the SEM image using Nano Measure 1.2. The unit of the average particle size is mean ± SD.

Conflict of Interest

The authors declare that they have no known competing financial interests or personal relationships that could have appeared to influence the work reported in this paper.

Author Contributions

W.F. and Z.S. conceived the concept and designed the experiments. W.F. and Z.S. prepared the materials, cells and conducted the measurements. W.F. and Z.S. drafted the manuscript. All authors discussed the data and revised the manuscript.

Data Availability Statement

Data will be made available on request.

Supporting Information

Supporting Information is available from the Wiley Online Library or from the author.

[1] Y. Zhang, B. Chen, D. Guan, M. Xu, R. Ran, M. Ni, W. Zhou, R. O'Hayre, Z. Shao, *Nature* **2021**, *591*, 246.

[2] J. H. Myung, D. Neagu, D. N. Miller, J. T. S. Irvine, *Nature* **2016**, *537*, 528.

[3] J. T. S. Irvine, D. Neagu, M. C. Verbraeken, C. Chatzichristodoulou, C. Graves, M. B. Mogensen, *Nat. Energy* **2016**, DOI: 10.1038/nenergy.2015.14.

[4] M. Papac, V. Stevanovi, A. Zakutayev, R. O'Hayre, *Nat. Mater.* **2021**, *20*, 301.

[5] P. Boldrin, N. P. Brandon, *Nat. Catal.* **2019**, *2*, 571.

[6] E. D. Wachsman, K. T. Lee, *Science* **2011**, *334*, 935.

[7] S. B. Adler, *Chem. Rev.* **2004**, *104*, 4791.

[8] S. Joo, O. Kwon, K. Kim, S. Kim, H. Kim, J. Shin, H. Y. Jeong, S. Sengodan, J. W. Han, G. Kim, *Nat. Commun.* **2019**, *10*, 697.

[9] Z. Sun, W. Fan, Y. Bai, K. Wu, Y. Cheng, *ACS Appl. Mater. Interfaces* **2021**, *13*, 29755.

[10] K. Develos-Bagarinao, T. Ishiyama, H. Kishimoto, H. Shimada, K. Yamaji, *Nat. Commun.* **2021**, DOI: 10.1038/s41467-021-24255-w.

[11] B. Hua, M. Li, Y. F. Sun, J. H. Li, J. L. Luo, *ChemSusChem* **2017**, *10*, 3333.

[12] G. Tsekouras, D. Neagu, J. T. S. Irvine, *Energ. Environ. Sci.* **2013**, *6*, 256.

[13] J. Zhou, T. H. Shin, C. Ni, G. Chen, K. Wu, Y. Cheng, J. T. S. Irvine, *Chem. Mater.* **2016**, *28*, 2981.

[14] W. W. Fan, Z. Sun, J. Wang, J. Zhou, K. Wu, Y. Cheng, *J. Power Sources* **2016**, *312*, 223.

[15] S. Choi, S. Sengodan, S. Park, Y. W. Ju, J. Kim, J. Hyodo, H. Y. Jeong, T. Ishihara, J. Shin, G. Kim, *J. Mater. Chem. A* **2016**, *4*, 1747.

[16] W. W. Fan, Z. Sun, Y. Bai, K. Wu, Y. H. Cheng, *ACS Appl. Mater. Interfaces* **2019**, *11*, 23168.

[17] W. W. Fan, Z. Sun, J. Zhou, K. Wu, Y. H. Cheng, *J. Power Sources* **2017**, *348*, 94.

[18] Y. Chen, B. de Glee, Y. Tang, Z. Wang, B. Zhao, Y. Wei, L. Zhang, S. Yoo, K. Pei, J. H. Kim, Y. Ding, P. Hu, F. F. Tao, M. Liu, *Nat. Energy* **2018**, *3*, 1042.

[19] B. Hua, M. Li, W. Pang, W. Tang, S. Zhao, Z. Jin, Y. Zeng, B. Shalchi Amirkhiz, J. L. Luo, *Chem* **2018**, *4*, 2902.

[20] M. Kothari, Y. Jeon, D. N. Miller, A. E. Pascui, J. Kilmartin, D. Wails, S. Ramos, A. Chadwick, J. T. S. Irvine, *Nat. Chem.* **2021**, *13*, 677.

[21] D. Neagu, G. Tsekouras, D. N. Miller, H. Menard, J. T. S. Irvine, *Nat. Chem.* **2013**, *5*, 916.

[22] C. P. Li, M. Qiu, R. Li, X. Li, M. Wang, J. He, G. Lin, L. Xiao, Q. Qian, Q. Chen, J. Wu, X. Li, Y.-W. Mai, Y. Chen, *Adv. Fiber Mater.* **2021**, *4*, 43.

[23] Q. F. Li, D. Yang, H. Chen, X. Lv, Y. Jiang, Y. Feng, X. Rui, Y. Yu, *SusMat* **2021**, *1*, 359.

[24] T. L. Zhu, H. E. Troiani, L. V. Mogni, M. F. Han, S. A. Barnett, *Joule* **2018**, *2*, 478.

[25] Y. H. Huang, R. I. Dass, Z. L. Xing, J. B. Goodenough, *Science* **2006**, *312*, 254.

[26] A. Zarkov, A. Stanulis, J. Sakaliuniene, S. Butkute, B. Abakeviciene, T. Salkus, S. Tautkus, A. F. Orliukas, S. Tamulevicius, A. Kareiva, *J. Sol-Gel Sci. Technol.* **2015**, *76*, 309.

[27] S. M. Logvinkov, G. D. Semchenko, D. A. Kobyzeva, V. I. Babushkin, *Refract. Ind. Ceram.* **2001**, *42*, 434.

[28] B. Schuh, B. Völker, J. Todt, N. Schell, L. Perrière, J. Li, J. P. Couzinié, A. Hohenwarter, *Acta Mater.* **2018**, *142*, 201.

[29] Y. G. Yao, Z. Huang, P. Xie, S. D. Lacey, R. J. Jacob, H. Xie, F. Chen, A. Nie, T. Pu, M. Rehwoldt, D. Yu, M. R. Zachariah, C. Wang, R. Shahbazian-Yassar, J. Li, L. Hu, *Science* **2018**, *359*, 1489.

[30] R. J. H. Voorhoeve, D. W. Johnson, J. P. Remeika, P. K. Gallagher, *Science* **1977**, *195*, 827.

[31] S. B. Liu, Q. X. Liu, J. L. Luo, *ACS Catal.* **2016**, *6*, 6219.

[32] J. Yu, R. Ran, Y. Zhong, W. Zhou, M. Ni, Z. Shao, *Energy Environ. Mater.* **2020**, *3*, 121.

[33] O. Celikbilek, C. A. Thieu, F. Agnese, E. Calì, C. Lenser, N. H. Menzler, J. W. Son, S. J. Skinner, E. Djurado, *J. Mater. Chem. A* **2019**, *7*, 25102.

[34] I. Jang, S. Kim, C. Kim, H. Yoon, T. Song, *J. Power Sources* **2018**, *392*, 123.

[35] Z. Q. Cao, Y. Zhang, J. Miao, Z. Wang, Z. Lü, Y. Sui, X. Huang, W. Jiang, *Int. J. Hydrogen Energy* **2015**, *40*, 16572.

[36] R. Martínez-Coronado, A. Aguadero, D. Pérez-Coll, L. Troncoso, J. A. Alonso, M. T. Fernández-Díaz, *Int. J. Hydrogen Energy* **2012**, *37*, 18310.

[37] W. D. Li, Y. Cheng, Q. Zhou, T. Wei, Z. Li, H. Yan, Z. Wang, X. Han, *Ceram. Int.* **2015**, *41*, 12393.

[38] D. Papargyriou, J. T. S. Irvine, *Solid State Ion.* **2016**, *288*, 120.

[39] Y. F. Sun, J. H. Li, L. Cui, B. Hua, S. H. Cui, J. Li, J. L. Luo, *Nanoscale* **2015**, *7*, 11173.

[40] D. E. Fowler, A. C. Messner, E. C. Miller, B. W. Slone, S. A. Barnett, K. R. Poeppelmeier, *Chem. Mater.* **2015**, *27*, 3683.

[41] L. F. Chen, J. A. Wang, M. A. Valenzuela, X. Bokhimi, D. R. Acosta, O. Novaro, *J. Alloys Compd.* **2006**, *417*, 220.

[42] Y. F. Sun, Y. Q. Zhang, J. Chen, J. H. Li, Y. T. Zhu, Y. M. Zeng, B. S. Amirkhiz, J. Li, B. Hua, J. L. Luo, *Nano Lett.* **2016**, *16*, 5303.

[43] Y. F. Sun, J. H. Li, L. Cui, B. Hua, S. H. Cui, J. Li, J. L. Luo, *Nanoscale* **2017**, *9*, 947.

[44] A. Leonide, V. Sonn, A. Weber, E. Ivers-Tiffée, *J. Electrochem. Soc.* **2008**, *155*, B36.

[45] M. F. Camellone, F. N. Ribeiro, L. Szabova, Y. Tateyama, S. Fabris, *J. Am. Chem. Soc.* **2016**, *138*, 11560.

[46] M. Cargnello, V. V. T. Doan-Nguyen, T. R. Gordon, R. E. Diaz, E. A. Stach, R. J. Gorte, P. Fornasiero, C. B. Murray, *Science* **2013**, *341*, 771.

[47] H. Han, J. Park, S. Y. Nam, K. J. Kim, G. M. Choi, S. S. P. Parkin, H. M. Jang, J. T. S. Irvine, *Nat. Commun.* **2019**, DOI: 10.1038/s41467-019-09395-4.

[48] O. Kwon, S. Sengodan, K. Kim, G. Kim, H. Y. Jeong, J. Shin, Y.-W. Ju, J. W. Han, G. Kim, *Nat. Commun.* **2017**, DOI: 10.1038/ncomms15967.

[49] D. Neagu, V. Kyriakou, I. L. Roiban, M. Aouine, C. Tang, A. Caravaca, K. Kousi, I. Schreur-Piet, I. S. Metcalfe, P. Vernoux, M. C. M. van de Sanden, M. N. Tsampas, *ACS Nano* **2019**, *13*, 12996.

[50] Y. Zhu, J. Dai, W. Zhou, Y. Zhong, H. Wang, Z. Shao, *J. Mater. Chem. A* **2018**, *6*, 13582.

[51] H. Y. Zhu, R. J. Kee, V. M. Janardhanan, O. Deutschmann, D. G. Goodwin, *J. Electrochem. Soc.* **2005**, *152*, 2427.

[52] Y. Choi, S. K. Cha, H. Ha, S. Lee, H. K. Seo, J. Y. Lee, H. Y. Kim, S. O. Kim, W. C. Jung, *Nat. Nanotechnol.* **2019**, *14*, 245.

[53] K. J. Kim, M. K. Rath, H. H. Kwak, H. J. Kim, J. W. Han, S. T. Hong, K. T. Lee, *ACS Catal.* **2019**, *9*, 1172.